

Article

Red-Emitting Hybrid Based on Eu^{3+} -dbm Complex Anchored on Silica Nanoparticles Surface by Carboxylic Acid for Biomarker Application

João A. O. Santos ^{1,2,3} , Alessandra M. G. Mutti ^{1,2}, Airton G. Bispo-Jr ³ , Ana M. Pires ^{1,2,3}  and Sergio A. M. Lima ^{1,*} 

¹ School of Technology and Sciences, São Paulo State University (Unesp), Presidente Prudente, SP 19060-900, Brazil; joao.antonio@unesp.br (J.A.O.S.); alegarbosamutti@gmail.com (A.M.G.M.); ana.maria@unesp.br (A.M.P.)

² Institute of Biosciences, Humanities and Exact Sciences, São Paulo State University (Unesp), São José do Rio Preto SP 15054-000, Brazil

³ Institute of Chemistry, São Paulo State University (Unesp), Araraquara SP 14800-900, Brazil; airton.germano.junior@gmail.com

* Correspondence: sergio.lima@unesp.br; Tel.: +55-18-3229-5752

Received: 3 October 2020; Accepted: 10 November 2020; Published: 2 December 2020



Abstract: Luminescent organic-inorganic hybrids containing lanthanides (Ln^{3+}) have been prominent for applications such as luminescent bio-probes in biological assays. In this sense, a luminescent hybrid based on dense silica (SiO_2) nanospheres decorated with Eu^{3+} β -diketonate complexes using dibenzoylmethane (Hdbm) as a luminescent antenna was developed by using a hierarchical organization in four steps: (i) anchoring of 3-aminopropyltriethoxysilane (APTES) organosilane on the SiO_2 surface, (ii) formation of a carboxylic acid ligand, (iii) coordination of Eu^{3+} to the carboxylate groups and (iv) coordination of dbm^- to Eu^{3+} . The hybrid structure was elucidated through the correlation of thermogravimetry, silicon nuclear magnetic resonance and photoluminescence. Results indicate that the carboxylic acid- Eu^{3+} -dbm hybrid was formed on the surface of the particles with no detectable changes on their size or shape after all the four steps (average size of 32 ± 7 nm). A surface charge of -27.8 mV was achieved for the hybrid, assuring a stable suspension in aqueous media. The Eu^{3+} complex provides intense red luminescence, characteristic of Eu^{3+} $^5\text{D}_0 \rightarrow ^7\text{F}_J$ electronic transitions, with an intrinsic emission quantum yield of 38%, even in an aqueous suspension. Therefore, the correlation of luminescence, structure, particle morphology and fluorescence microscopy images make the hybrid promising for application in bioimaging.

Keywords: luminescent material; functionalization; lanthanide; β -diketone; SiO_2 ; bioimaging

1. Introduction

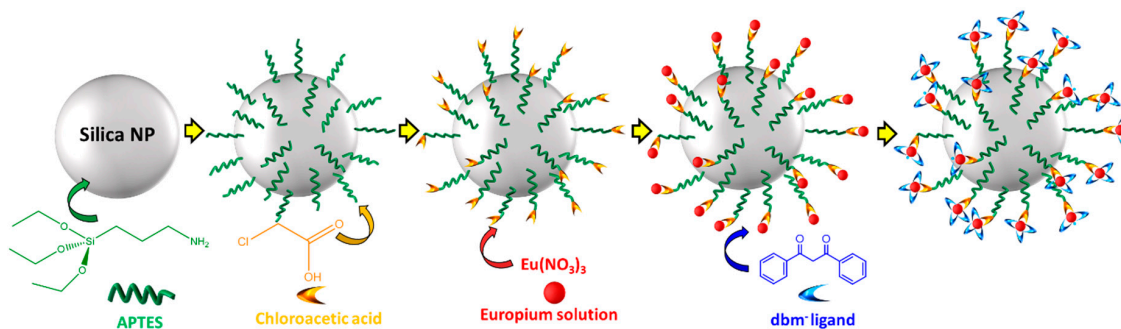
Clinical diagnosis by imaging is expanding due to the development of sensitive and non-invasive techniques such as confocal or fluorescence microscopy, appearing as powerful tools for exploratory analyses of several biological processes and internal structural information of healthy and cancerogenous cells [1–3]. Among several biomaterials applied in bioimaging, luminescent biomarkers are widely used as contrast agents for in vivo and in vitro, clinical assays, acting as bio-probes responsible by imaging and clinical information of the cellular environment [4,5]. Therefore, new strategies towards the development and improvement of the luminescent and structural features of such bio-probes are of large social relevance.

Luminescent biomarkers reported in the literature can be classified in different categories, that is, organic dyes and fluorescent proteins [6], quantum dots [7], metallic nanoparticles [8], carbon dots [9]

and Ln^{3+} or metallic ions in complexes or in inorganic hosts [10–12]. Each of those materials features chemical, physical and biological peculiarities that bring several advantages and disadvantages for use in cellular imaging [13].

In this sense, Eu^{3+} β -diketonate complexes excel for bioimaging [2,5,12,14] due to several features such as: (i) efficient antenna effect played by β -diketonates to sensitize the Eu^{3+} luminescence, rendering biomarkers displaying relatively-high intrinsic emission quantum yield, (ii) excitation bands shifted to lower energy regions (near-UV or blue), (iii) large pseudo-Stokes shift, (iv) narrow Eu^{3+} emission bands within the red spectral region that arise from intraconfigurational $f-f$ electronic transitions, leading to bright and pure red light emission, (v) emission within the biological window where light is less scattered and absorbed and easily differentiate from the biological autofluorescence, typically in the blue-green region [2] and (vi) long emission lifetime, within the 10^{-6} – 10^{-3} s range, favoring time-resolved luminescence methods to time-differentiate the cell autofluorescence, whose luminescence lifetime is typically shorter [15]. On the other hand, some drawbacks such as poor photostability upon UV excitation and low solubility in water need to be addressed for biological assays [16].

Such shortcomings have been minimized over the immobilization of complexes in inorganic nanoparticles, for example, silica (SiO_2) [12,17,18], clays [19], oxides [20], metals [21] or core-shell systems [22], making of these hybrid materials processed as stable colloidal suspensions displaying desirable luminescence and improved photostability. Moreover, the immobilization of the complex on the surface allows the nanoparticle internalization by cells, introducing a considerable number of luminescent centers within them, decreasing the dosage necessary to get first-rate clinical images. Among several support materials for the luminescent complex immobilization, SiO_2 stands out as a biocompatible and non-toxic material for most cell lines due to the ease surface modification, entailing versatility for biofunctionalization by a substantial number of molecules [23–25]. Several methodologies can be employed to modify dense or mesoporous SiO_2 surface to fabricate biomarkers, such as, complexes impregnation into the pores [26,27], encapsulation within the nanoparticle [28–30], immobilization by electrostatic interaction (cationic and anionic complexes) [31] or covalently-anchor onto the nanoparticle surface [12,32–34]. In this last case, the covalent bond avoids the complexes release in the cell environment and luminescence quenching compared to encapsulated architectures. The covalent bonding of the complexes on the silica surface is mediated by their previous modification with organosilanes that contain chelating groups (e.g., Schiff base, carboxylic acids, esters, ketones, pyridines), capable of binding to the first coordination sphere of the metal. In this sense, functionalization with a carboxylic acid, one of the least reported in the literature, draws attention due to the great versatility of this group, adding interesting biological properties to the material [35] such as increased biocompatibility, good colloidal stability [36], the possibility of conjugation with biomolecules [37] and an excellent chelating group for the coordination of several metals [38]. Accordingly, herein a step-by-step method, Scheme 1, is introduced to synthesize a hierarchical red-emitting hybrid based on covalent bonds of Eu^{3+} - β -diketonates on the surface of decorated dense SiO_2 nanoparticles assisted by monocarboxylic ligands featuring bioimaging application.



Scheme 1. Scheme illustrating the sequence of reaction steps for the luminescent hybrid production.

2. Materials and Methods

2.1. Materials

Tetraethylorthosilicate (TEOS) (Fluka, 99%), ammonium hydroxide (Synth, 24.26%), hydrochloric acid (Synth, 37%), methanol (Synth, 99.8%), ethanol (Synth, 99.5%), APTES (Synth, 98%), ninhydrin (Aldrich, 97%), chloroacetic acid (Sigma-Aldrich, 99.5%), potassium carbonate (Cinética, 99%), sodium hydroxide (Cinética, 97%), potassium methoxide (Aldrich, 97%), europium oxide (Aldrich, 99.99%) and Hdbm (Synth, 99.8%) were used without any further purification.

2.2. Synthesis of Silica Nanoparticles

For the synthesis of dense silica nanoparticles, the alkali-catalyzed sol-gel methodology (NH_4OH) was used [39]. For this, in a beaker (100 mL), deionized water (5.59 mL), NH_4OH (1.37 mL) and methanol (32.80 mL) were added. The mixture was kept under magnetic stirring at 25 °C (5 min); TEOS (3.60 mL) was slowly added and the solution was kept under stirring for 90 min. Sequentially, the stirring was stopped and the suspension rested for 12 h. The powder suspension was washed 3° times with methanol (12 mL) and centrifuged at 3800 rpm for 20 min. Finally, the sample was dried in a desiccator and afterward in an oven at 70 °C for 24 h. The silica sample synthesized will be hereafter labeled as S_1 . At the end of the process, 698.2 mg of S_1 was obtained. Assignments for S_1 Fourier Transform Infrared (FTIR) spectrum (KBr, cm^{-1}): 3256 $\nu(\text{O-H})$, 1630 $\delta(\text{O-H}, \text{H}_2\text{O})$, 1106 $\nu_{\text{as}}(\text{Si-O-Si})$, 949 $\nu(\text{Si-O-H})$, 800 $\nu_{\text{s}}(\text{Si-O-Si})$, 470 $\delta_{\text{s}}(\text{Si-O-Si}, \text{dense network of } \text{SiO}_4^{4-} \text{ tetrahedra})$ [40]. Attribution for S_1 $^{29}\text{Si-NMR } Q^n$ (ppm; %): Q^4 (−111; 68.04), Q^3 (−102; 27.99), Q^2 (−93; 3.97).

2.3. Amino-Functionalization

In a beaker (100 mL), 0.5500 g of S_1 was suspended in ethanol (35 mL) and kept in an ultrasonic bath (15 min). After that, APTES ethanolic solution was prepared by adding APTES (2.19 mL) in ethanol (15 mL). This solution was transferred to the beaker containing the S_1 suspension under magnetic stirring and the silanization reaction proceeded vigorously at 25 °C (3 h). Then, the amino-functionalized nanoparticles were washed 3 times with ethanol (15 mL) and centrifuged at 3800 rpm (10 min). The powder was dried in a desiccator and then oven-dried at 70 °C (6 h), yielding a mass of 0.5210 g that hereafter will be named as $S_1\text{N}$. Assignments for $S_1\text{N}$ FTIR spectrum (KBr, cm^{-1}): 3243 $\nu(\text{O-H})$, 1630 $\delta(\text{O-H}, \text{H}_2\text{O})$, 1545 $\delta(\text{N-H})$, 1103 $\nu_{\text{as}}(\text{Si-O-Si})$, 951 $\nu(\text{Si-O-H})$, 803 $\nu_{\text{s}}(\text{Si-O-Si})$, 471 $\delta_{\text{s}}(\text{Si-O-Si}, \text{dense network of } \text{SiO}_4^{4-} \text{ tetrahedra})$ [40,41]. Attribution for $S_1\text{N}$ $^{29}\text{Si-NMR } Q^n$ and T^n (ppm; %): Q^4 (−111; 70.27), Q^3 (−102; 24.05), Q^2 (−93; 3.55), T^3 (−67; 0.25), T^2 (−60; 1.87).

2.4. Carboxyl-Functionalization

The carboxyl-functionalization was adapted from Reference [42], in which 0.2987 g of $S_1\text{N}$ —2.26 mmol of $-\text{NH}_3^+$ estimated by colorimetric method using ninhydrin [43]—was suspended in deionized water (20 mL) followed by the addition of K_2CO_3 (1.13 mmol) and left in ultrasound (15 min); after this time, the suspension was transferred to a round-bottom flask (50 mL). Thereafter, chloroacetic acid (4.52 mmol) was solubilized in deionized water (3 mL) and neutralized with K_2CO_3 (1.13 mmol); this solution was transferred to the reactional round-bottom flask. The reaction proceeded upon vigorous magnetic stirring at 60 °C (24 h). At the end of this time, the nanoparticles were washed twice with deionized water and twice with an aqueous solution of HCl ($10^{-3} \text{ mol}\cdot\text{L}^{-1}$). Finally, the sample was dried in a desiccator and then oven-dried at 70 °C, yielding 0.2449 g of the henceforth called $S_1\text{NC}$ sample. The carboxylic groups were quantified indirectly via the ninhydrin method [43]. Assignments for the $S_1\text{NC}$ FTIR spectrum (KBr, cm^{-1}): 3452 $\nu(\text{O-H})$, 2959 and 2928 $\nu_{\text{as}}(\text{C-H}, \text{CH}_2)$, 2855 $\nu_{\text{s}}(\text{C-H}, \text{CH}_2)$, 1743 $\nu(\text{C}=\text{O})$, 1630 $\delta(\text{O-H}, \text{H}_2\text{O})$, 1105 $\nu_{\text{as}}(\text{Si-O-Si})$, 949 $\nu(\text{Si-O-H})$, 800 $\nu_{\text{s}}(\text{Si-O-Si})$, 470 $\delta_{\text{s}}(\text{Si-O-Si}, \text{dense network of } \text{SiO}_4^{4-} \text{ tetrahedra})$ [40].

After this step, the carboxylate-ligand salt ($-\text{COO}^-\text{Na}^+$) was prepared to promote the Eu^{3+} coordination. For that, the $S_1\text{NC}$ nanoparticles were suspended in water followed by the stoichiometric

addition of NaOH (1 mmol·L⁻¹). The solvent was evaporated and the sample was oven-dried at 80 °C. Assignments for the salt S₁NC FTIR spectrum (KBr, cm⁻¹): 3259 ν(O–H), 1524 ν_{as}(COO⁻), 1414 ν_s(COO⁻), 1630 δ(O–H, H₂O), 1103 ν_{as}(Si–O–Si), 949 ν(Si–O–H), 800 ν_s(Si–O–Si), 471 δ_s(Si–O–Si, dense network of silicon tetrahedrons SiO₄⁴⁻) [40,44].

2.5. Coordination of Eu³⁺ to -COO⁻ Groups

In a round-bottom flask, 60 mg of S₁NC—corresponding to 0.422 mmol of COO⁻ groups—was suspended with 10 mL of ethanol in ultrasound (5 min), then 0.464 mmol of Eu(NO₃)₃ in water (0.0455 mol·L⁻¹) was added. The reaction was kept under stirring (5 h) at 50 °C by using a reflux system. The sample was then washed 3 times with ethanol (15 mL) and centrifuged at 3800 rpm (10 min, 25 °C). Finally, the powder was dried in a desiccator and in an oven (6 h), producing 61.1 mg of the hereafter labeled S₁-[Eu] sample. Assignments for the S₁-[Eu] FTIR spectrum (KBr, cm⁻¹): 3415 ν(O–H), 2924 ν_{as}(C–H, CH₂), 2852 ν_s(C–H, CH₂), 1524 ν_{as}(COO⁻), 1414 ν_s(COO⁻), 1635 δ(O–H, H₂O), 1385 ν(NO₃⁻), 1107 ν_{as}(Si–O–Si), 951 ν(Si–O–H), 798 ν_s(Si–O–Si), 467 δ_s(Si–O–Si, dense network of SiO₄⁴⁻ tetrahedra) [40,45].

2.6. Displacement of Coordination Water Molecules by dbm⁻ Ligands

The synthesis methodology was adapted from Mutti [12]. In a beaker (50 mL), 40 mg of S₁-[Eu] was transferred and suspended in ethanol (10 mL). The suspension was kept under an ultrasonic bath and then, it was transferred to a round-bottom flask (100 mL). The ligand Hdbm (195.5 mg, 0.87 mmol) was separately deprotonated with CH₃OK (0.87 mmol in 10 mL of ethanol) and this solution was transferred dropwise to the reactional medium, that was kept under magnetic stirring at 50 °C (6 h). The suspension was washed 3 times with ethanol (15 mL) and centrifuged at 3800 rpm (10 min, 25 °C). Finally, the powder was dried in a desiccator and in an oven at 70 °C (6 h), leading to 45.5 mg of the sample, hereafter named S₁-[Eu(dbm)]. Assignments for the S₁-[Eu(dbm)] FTIR spectrum (KBr, cm⁻¹): 3419 ν(O–H), 3060 ν(C–H, aromatic), 2959 and 2922 ν_{as}(C–H, CH₂), 2851 ν_s(C–H, CH₂), 1596 ν(C = O), 1548 ν_s(C = C), 1522 ν_s(C = O), 1478 and 1456 δ_{as}(C–H, aromatic), 1222 and 602 δ(C–H, aromatic)_{in plane}, 1099 ν_{as}(Si–O–Si), 957 ν(Si–O–H), 799 ν_s(Si–O–Si), 745 and 718 ν(C–H, aromatic), 683 δ(C–H, aromatic)_{out plane}, 617 ν(Eu–O), 467 δ_s(Si–O–Si, dense network of SiO₄⁴⁻ tetrahedra) [27,40].

2.7. Instrumentation

Images of samples were achieved from a Field Emission Gun Scanning Electron Microscopy (SEM FEG) JEOL model 7500F using an ethanolic suspension of nanoparticles dropped onto a Si substrate, sequentially coated with carbon by sputtering. Histograms were constructed by counting 100 nanoparticles using ImageJ (version 1.53e) [46]. FTIR spectra in KBr pellets were carried out in a Bruker model Tensor 27 spectrophotometer from 400–4000 cm⁻¹ and increment of 4 cm⁻¹. The –NH₂ quantification was performed by using the ninhydrin colorimetric test [43] based on the absorption of Ruhemann's purple compound using a Shimadzu model UV-1800 spectrophotometer (double beam) and ethanolic ninhydrin solution 5% (wt./v) as reference. Silicon Nuclear Magnetic Resonance (²⁹Si {¹H} CP/MAS NMR and ²⁹Si MAS NMR) spectra were obtained on a Bruker Avance III HD 400 WB (9.4 T) spectrometer, with a 4 mm cross-polarization/magic-angle spinning (CP/MAS) probe and a maximum rotation frequency of 15 kHz, operating at temperatures between –140–150 °C. Thermogravimetry was carried out in a SDT-Q600TA equipment, from 25–1000 °C in Pt crucible, a heating rate of 10 °C/min upon circulating air atmosphere (100 mL/min). Zeta potential of the particles was measured in a Zetasizer Nano Series, model Nano-ZS, equipment from Malvern Instruments, in triplicate by using a suspension of the particles in phosphate buffer (0.01 mol/L, pH = 7.64). The excitation and emission spectra were measured in a Horiba Jobin Yvon, model Fluorolog-3 spectrofluorometer—continuous Xe lamp (450 W) with double excitation and emission monochromator and an R 928 Hamamatsu photomultiplier. Time-resolved spectroscopy was carried out in a phosphorimeter equipped with a Xe

bulb (5 J/pulse). Fluorescence microscopy images of CHO-k1 cells were performed in a Nikon Confocal Microscope model C2/C2si, equipped with an inverted microscope system (Eclipse Ti-E) capable of obtaining fluorescence and confocal images using 405 and 561 nm lasers. The preparation protocol of glass slides for fluorescence microscopy analysis is described in Note S1 of Supplementary Material.

3. Results and Discussion

3.1. Structure and Morphology

SEM FEG images, Figure 1, confirm that spheroidal-shaped nanoparticles were obtained after the synthesis and that step-by-step process does not lead to any change of the particle size (average size of 32 ± 7 nm determined by Figure S1A,B), suggesting none leaching of the SiO₂ surface and that the method is topotactic. The chemical mapping of the S₁-[Eu(dbm)] hybrid surface evaluated by Energy-Dispersive Spectroscopy (EDS), Figure S1C–E, confirms that Eu³⁺ is evenly distributed throughout the surface and remains anchored even after successive washing and centrifugation processes.

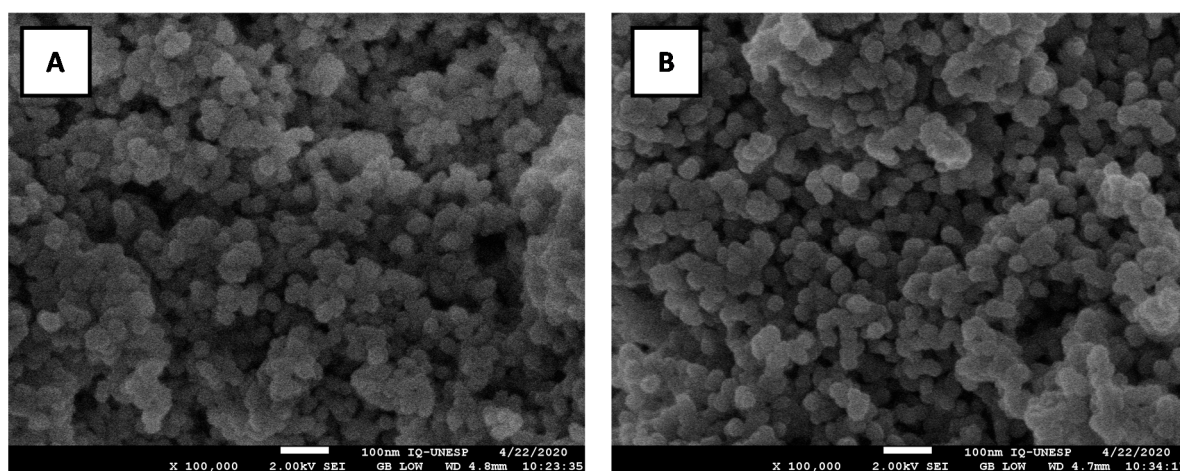


Figure 1. SEM FEG of (A) S₁ and (B) S₁-[Eu(dbm)].

The chemical bond formation of the S₁-[Eu(dbm)] hybrid was elucidated by Fourier transform infrared (FTIR), Figure S2. S₁-[Eu(dbm)] FTIR spectrum exhibits all the characteristic SiO₂ vibrational modes. The anchoring of APTES on the SiO₂ surface was confirmed by the vibrational mode at 1545 cm⁻¹ related to the N-H bending of primary amines which vanishes in the S₁NC sample due to the conversion of the N-H group into a secondary amine [40,41]. S₁NC also shows the $\nu(\text{C}=\text{O})$ stretch at 1743 cm⁻¹ assigned to the COOH group and after the deprotonation, the vibrational modes at 1524 cm⁻¹ and 1414 cm⁻¹ were attributed to the antisymmetric (ν_{as}) and symmetric (ν_{s}) stretching vibrations of the COO⁻ group, respectively [40]. For the S₁-[Eu] sample, those vibrational modes shift to 1506 cm⁻¹ and 1419 cm⁻¹ due to the coordination of Eu³⁺ to the COO⁻ group. The shift to lower wavenumbers (see Table S1) also ensures that Eu³⁺ coordinates itself to the COO⁻ group in a bidentate way according to the literature [44]. Furthermore, S₁-[Eu] also displays a band at 1385 cm⁻¹ characteristics of free NO₃⁻, probably as counter-ion and another one at 875 cm⁻¹ assigned to NO₃⁻ coordinated to Eu³⁺ [47]. Finally, the Eu³⁺ coordination to dbm⁻ ligands was confirmed by the characteristic vibrational modes of the ligands (C-H stretching of aromatic rings at 3060 cm⁻¹ and other vibrational modes of organic groups below 1600 cm⁻¹) and the Eu-O stretching at 617 cm⁻¹ [27].

The covalent bond of APTES onto the SiO₂ surface was investigated by using ²⁹Si MAS NMR, Figure 2, where Q⁴ (-111 ppm), Q³ (-101 ppm) and Q² (-93 ppm) groups were identified. The Q⁴ group is assigned to Si(O-Si)₄ characteristic of the internal network of SiO₂ particles, while Q³ and Q² groups are associated with Si(O-Si)₃(OH) and Si(O-Si)₂(OH)₂, respectively [30]. The APTES anchorage on the SiO₂ surface was confirmed by the presence of T² (-60 ppm) and T³ (-67 ppm) groups in the NMR spectrum, Figure 2B, which are characteristics of R-Si(O-Si)₂(OH) and R-Si(O-Si)₃, respectively,

indicating that APTES bonds itself to the silica surface through bi- or tridentate modes, as illustrated in Figure 2D. From the area of the peaks in the ^{29}Si NMR spectra, the mol% of Q^n and T^n groups are determined before and after the APTES functionalization, Table 1. While the amount of Q^4 groups represents around 68 mol% for S_1 , this amount increases up to 70 mol% for S_1N . The amount of Q^2 groups is almost invariant but the amount of Q^3 decreases from $\sim 28\%$ to about 24%, for S_1 and S_1N , respectively. Since the Q^3 group is bonded to one hydroxyl molecule, this variation indicates a decrease of 14% of the hydroxyl groups on the surface of the silica after the amino-functionalization. The amount of APTES molecules anchored onto the silica surface can be determined through the integration of T^n groups, that is 2.12 mol%; although it represents a small percentage, it is enough to enable the formation of complexes at the following steps, as indicated by FTIR and to obtain a highly emissive material as will be discussed later. To confirm the presence of T^n groups, it was performed the ^{29}Si NMR at CP/MAS mode, which intensify signals associated with silicon atoms neighboring hydrogen atoms, Figure 2C.

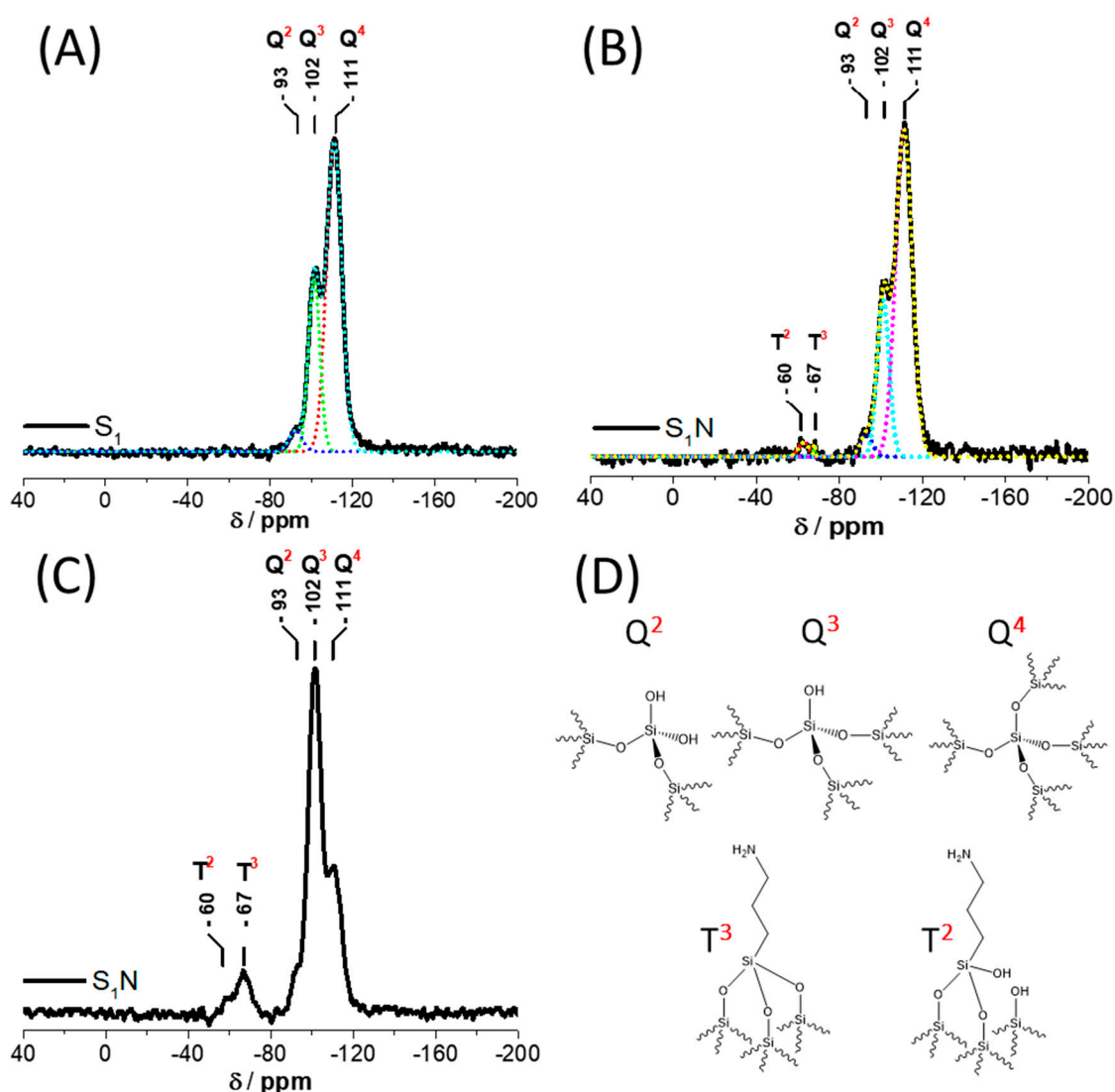


Figure 2. ^{29}Si MAS NMR spectra of (A) S_1 and (B) S_1N ; the dashed lines represent deconvoluted curves obtained by using a Gaussian function. (C) ^{29}Si $\{^1\text{H}\}$ CP/MAS NMR spectrum of S_1N . (D) Illustration of $\text{Q}^{2,3,4}$ and $\text{T}^{2,3}$ groups.

Table 1. Percentage of groups obtained by deconvolution (Gaussian fitting) of ^{29}Si NMR MAS spectra before and after the amino-functionalization process.

Groups	S ₁ Sample	S ₁ N Sample
	Group Quantity in mol%	Group Quantity in mol%
Q ⁴	68.04 ± 0.25	70.27 ± 0.40
Q ³	27.99 ± 0.34	24.05 ± 0.63
Q ²	3.97 ± 0.24	3.55 ± 0.43
T ³	-	0.25 ± 0.06
T ²	-	1.87 ± 0.17

The concentration of external amino groups ($-\text{NH}_2$) was quantitatively estimated by the ninhydrin colorimetric assay described in the experimental procedure [43]. As a first visual test, S₁N in ninhydrin solution becomes violet, confirming the presence of primary amines, Figure S3A. However, S₁NC in ninhydrin solution displayed a yellowish-orange color, suggesting that the conversion of primary amines to secondary amines (not identified by ninhydrin) reached high yield. From the calibration curve using the Rheumann's purple compound with a reliable absorbance at 578 nm, Figure S3B, the concentration of $-\text{NH}_2$ groups was 7.58 mmol/g and 0.55 mmol/g for S₁N and S₁NC, respectively. From the difference between the concentration of $-\text{NH}_2$ groups in both samples and assuming that $-\text{NH}_2$ groups were converted to $\text{NH}(\text{CH}_2\text{COOH})$, the concentration of carboxyl groups in the S₁NC sample is estimated as 7.03 mmol/g—corresponding to 90% of conversion.

Modifications on the SiO₂ nanoparticle surface was investigated by thermogravimetry. Two major thermal events are seen in Figure 3, the first that occurs around 200 °C is the release of water molecules adsorbed onto the SiO₂ surface by hydrogen bondings involving silanol groups and the second event beginning at 200 °C is associated to the dehydroxylation silanol groups at the surface of the particles. After the functionalization processes, the combustion of organic matter anchored on the sample surface also contributes to the second thermal event. As expected, there is an increase in the weight loss of the second process, Table S2, due to the organic portion coming from the functionalization steps. The exact ending temperature of each process is indicated in Differential Thermogravimetry curves (DTG), Figure S4.

The surface charge of the hybrid in aqueous solution is a meaningful parameter considering its application as a biomarker and it was evaluated by zeta potential (ZP, at pH = 7.64, close to the physiological pH), Figure 4. For S₁, at this pH value, the ZP is negative due to the deprotonation of silanol groups on the particle surface while for S₁N, the $-\text{NH}_2$ groups are protonated ($-\text{NH}_3^+$), giving a positive charge. After the carboxyl functionalization step, S₁NC exhibits a negative charge due to the carboxyl group deprotonation, following the literature [48]. After the Eu^{3+} coordination to the carboxylate groups, ZP of S₁-[Eu] is lowered due to the formation of negatively charged complexes containing NO_3^- ligands according to FTIR data. Finally, the dbm^- coordination does not lead to further changes in the ZP since dbm^- replaces NO_3^- ligands and both anions have the same charge.

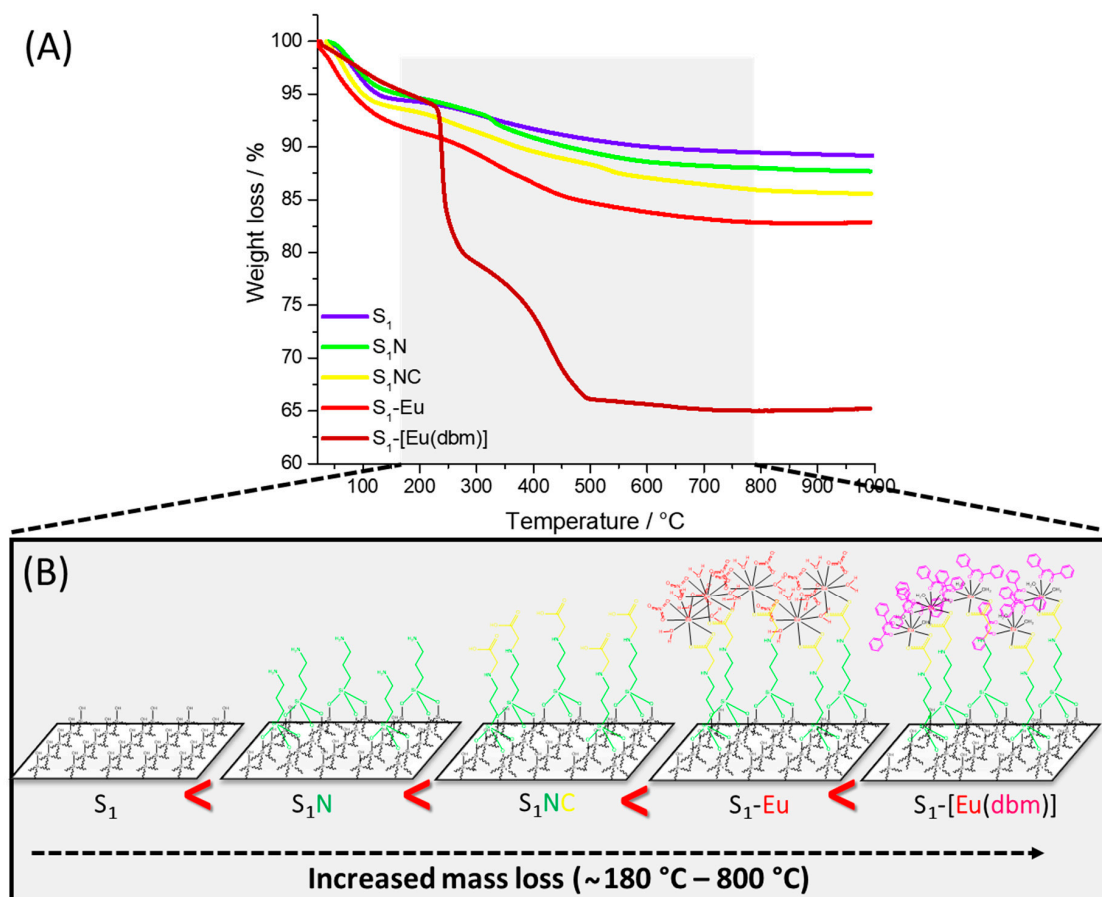


Figure 3. (A) Thermogravimetric curves of all samples obtained after each functionalization step. (B) Surface illustrative representation of all samples, elucidating the increase of organic matter losses during the second thermal event.

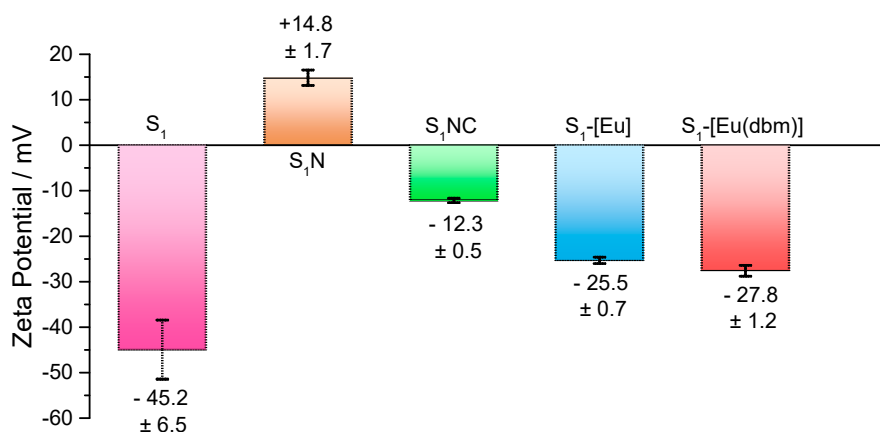


Figure 4. Zeta potential (pH = 7.64) for the particles synthesized in each functionalization step.

3.2. Luminescence

Considering the application of the hybrid as a biomarker, it is crucial to evaluate its luminescent features and for that, S₁NC, S₁-[Eu] and S₁-[Eu(dbm)] had their excitation and emission spectra measured, as can be seen in Figure 5. S₁NC displays broad excitation and emission bands peaking at 356 and 433 nm, respectively, which come from the SiO₂ intrinsic luminescence. One explanation in literature for the SiO₂ luminescence is related to the electron-hole recombination due to structural defects on the particle surface involving siloxane groups, generating defect-related electronic levels [49].

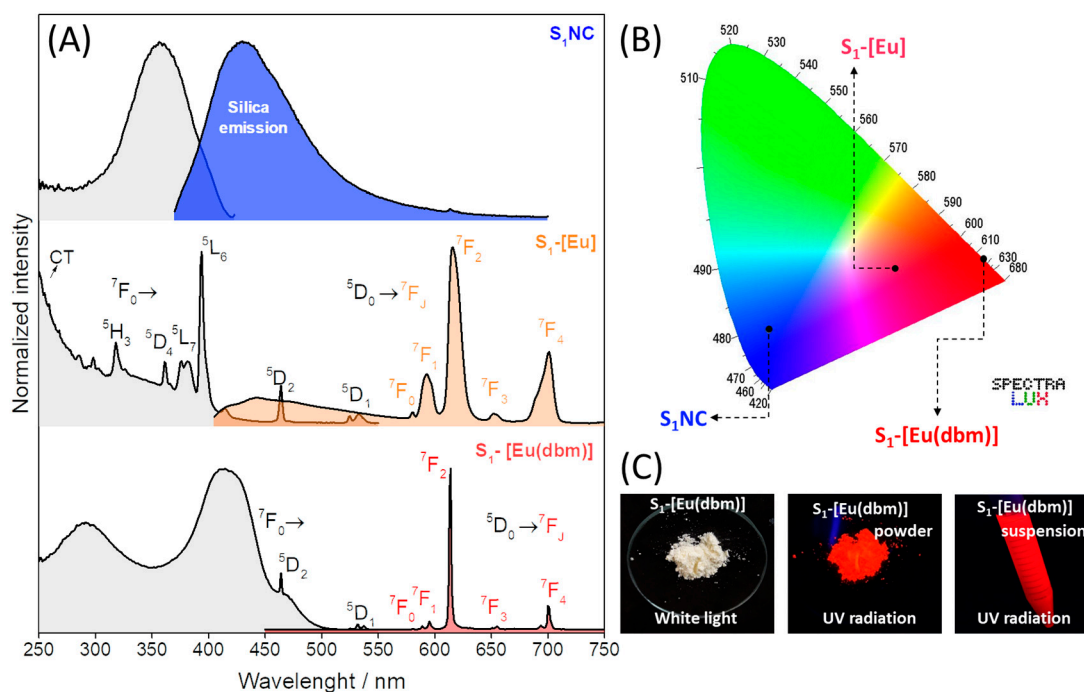


Figure 5. (A) Excitation and emission spectra (300 K) monitored at 433 and 356 nm for sample S_1 NC; 616 and 394 nm for sample S_1 -[Eu]; and 615 and 412 nm for sample S_1 -[Eu(dbm)], respectively. (B) 1931 CIE diagram of S_1 NC, S_1 -[Eu] S_1 -[Eu(dbm)] samples obtained from Reference [50]. (C) Photograph of S_1 -[Eu(dbm)] processed as powder or suspended in ethanol under white light and UV radiation (350 nm).

In the excitation spectrum of S_1 -[Eu], Figure 5A, the intraconfigurational $f-f$ electronic transitions of Eu^{3+} are observed [51], while an intense broad absorption band bellows 300 nm is associated to $\text{O}^{2-} \rightarrow \text{Eu}^{3+}$ charge transfer band (CT). Moreover, no excitation band associated with carboxylate groups is noticed, confirming its role in only anchoring Eu^{3+} to the SiO_2 surface. Upon 394 nm excitation ($\text{Eu}^{3+} 7F_0 \rightarrow 5L_6$ transition), the emission spectrum of S_1 -[Eu] is characterized by the typical $5D_0 \rightarrow 7F_{0-4}$ Eu^{3+} electronic transitions within the red spectral region overlapped to the SiO_2 -related broad emission band in the blue spectral region. The quite broad profile of the Eu^{3+} emission bands is associated with different Eu^{3+} local microsymmetries on the particle surface [16]. In this sample the intensity is lower due to the presence of coordinated water molecules, which acts as a quencher through multiphonon non-radiative processes due to O-H oscillators [52]. Similar results were found by Rocha [45] for Eu^{3+} incorporated into amorphous mesoporous SiO_2 .

To enhance the luminescence of S_1 -[Eu], dbm^- was coordinated to Eu^{3+} [27]. Its excitation spectra, Figure 5A, is dominated by broad and intense bands ranging 250–500 nm characteristic of dbm^- absorption, confirming that dbm^- sensitizes Eu^{3+} ion; some Eu^{3+} $f-f$ absorption transitions with lower intensity are also observed. Interestingly, the dbm^- excitation bands fulfill the blue/violet excitation range, ensuring that the hybrid may be excited by using lower energetic wavelengths than the traditional energy within the near-UV spectral window used to excite downshift hybrids, which is, from the biological point of view, disadvantageous since UV radiation is dangerous to live organisms submitted to in vivo or in vitro assays [5]. The addition of dbm^- ligand leads to an enhancement of the intensity of the final S_1 -[Eu(dbm)] hybrid compared to S_1 -[Eu], making the Eu^{3+} emission bands narrower.

It is well-known that Eu^{3+} may act as a spectroscopic probe since some of its $f-f$ transitions are sensitive to the ligand field around it, enabling further evaluations of Eu^{3+} local microsymmetry changes [53]. Specifically, the ratio between the emission band areas assigned to the forced electric dipole $5D_0 \rightarrow 7F_2$ transition and the magnetic dipole $5D_0 \rightarrow 7F_1$ transition enables evaluations of the

asymmetry of the Eu^{3+} local sites. This ratio increases from 4.0–12.0 after the dbm^- coordination leading to a symmetry-lowering around Eu^{3+} . This is an advantage since the ${}^5\text{D}_0 \rightarrow {}^7\text{F}_2$ transition has its oscillator strength increased in low-symmetric sites [51].

The hybrid emission color was quantified by the colorimetric point of view by using the Commission Internationale de L'éclairage (CIE) 1931 diagram, Figure 5B. The (x,y) color coordinate of S_1NC is (0.16, 0.16) within the blue spectral region with a dominant wavelength of 475 nm and color purity of 76%. After the Eu^{3+} coordination on the SiO_2 surface, the color emission of $\text{S}_1\text{-[Eu]}$ moves towards the pink spectral region (0.47,0.29) due to the color mixture of Eu^{3+} and SiO_2 emissions, with color purity of 29%. Finally, after the dbm^- coordination to Eu^{3+} , the $\text{S}_1\text{-[Eu(dbm)]}$ emission color dislocates to the red spectral region (0.68, 0.31) achieving 100% of color purity and dominant wavelength of 615 nm, confirming that the dbm^- coordination was a valuable strategy to enhance the emission color purity and red light emission of the hybrid, as it can be seen by naked eyes, Figure 5C.

To ensure that the Eu^{3+} emission can be differentiated from the SiO_2 emission in $\text{S}_1\text{-[Eu]}$, time-resolved emission spectra were carried out, Figure 6A, confirming that a delay of 50 μs is enough to eliminate the SiO_2 contribution to the emission spectrum. This delay time is close to the biological autofluorescence, demonstrating an advantage of using Ln^{3+} -based biomarkers, for these later have a much longer emission lifetime allowing to distinguish between the biological emission from the hybrid emission [54]. On the other hand, for the final $\text{S}_1\text{-[Eu(dbm)]}$ hybrid, time-resolved spectroscopy is not necessary since the Eu^{3+} sensitization by dbm^- makes its emission much more intense than the SiO_2 band even in steady-state acquisition mode, Figure 5A.

The photokinetic features of $\text{S}_1\text{-[Eu]}$ and $\text{S}_1\text{-[Eu(dbm)]}$ hybrids were further elucidated by emission decay curves, Figure 6B and the ${}^5\text{D}_0$ excited state lifetimes (τ) are listed in Table 2. Since the Eu^{3+} ions can be inserted in several chemical environments when coordinated on the surface of the silica particle, we determined τ through the Inokuti–Hirayama model shown in Equation (1), which gives us a mean value of all excited-state lifetimes. As the ${}^5\text{D}_0$ state lifetime depends on radiative (A_{rad}) and nonradiative (A_{nrad}) decay rates, $\tau = (A_{\text{rad}} + A_{\text{nrad}})^{-1}$, it is possible to get the intrinsic emission quantum yield ($\phi_{\text{Ln}}^{\text{Ln}}$) of Eu^{3+} — $\phi_{\text{Ln}}^{\text{Ln}} = A_{\text{rad}} / (A_{\text{rad}} + A_{\text{nrad}})$ [55]. In this case, A_{rad} ($A_{\text{rad}} = \sum A_{0j}$) is determined from the emission spectrum by using Equation (2).

$$\tau = \frac{\int_0^\infty I(t)t dt}{\int_0^\infty I(t) dt} \quad (1)$$

$$A_{0\lambda} = A_{01} \left(\frac{S_{0j}}{S_{01}} \right) \left(\frac{\sigma_{01}}{\sigma_{0j}} \right), \quad (2)$$

where $I(t)$ is the emission intensity at a time t , $A_{01} = (0.31 \times 10^{-11}) \times \eta^3 \times \sigma_{0 \rightarrow 1}^3$ and σ_{0j} and S_{0j} are the energy barycenter and the integrated intensity of the ${}^5\text{D}_0 \rightarrow {}^7\text{F}_j$ transitions, respectively and η is the refractive index of SiO_2 (1.435) [56].

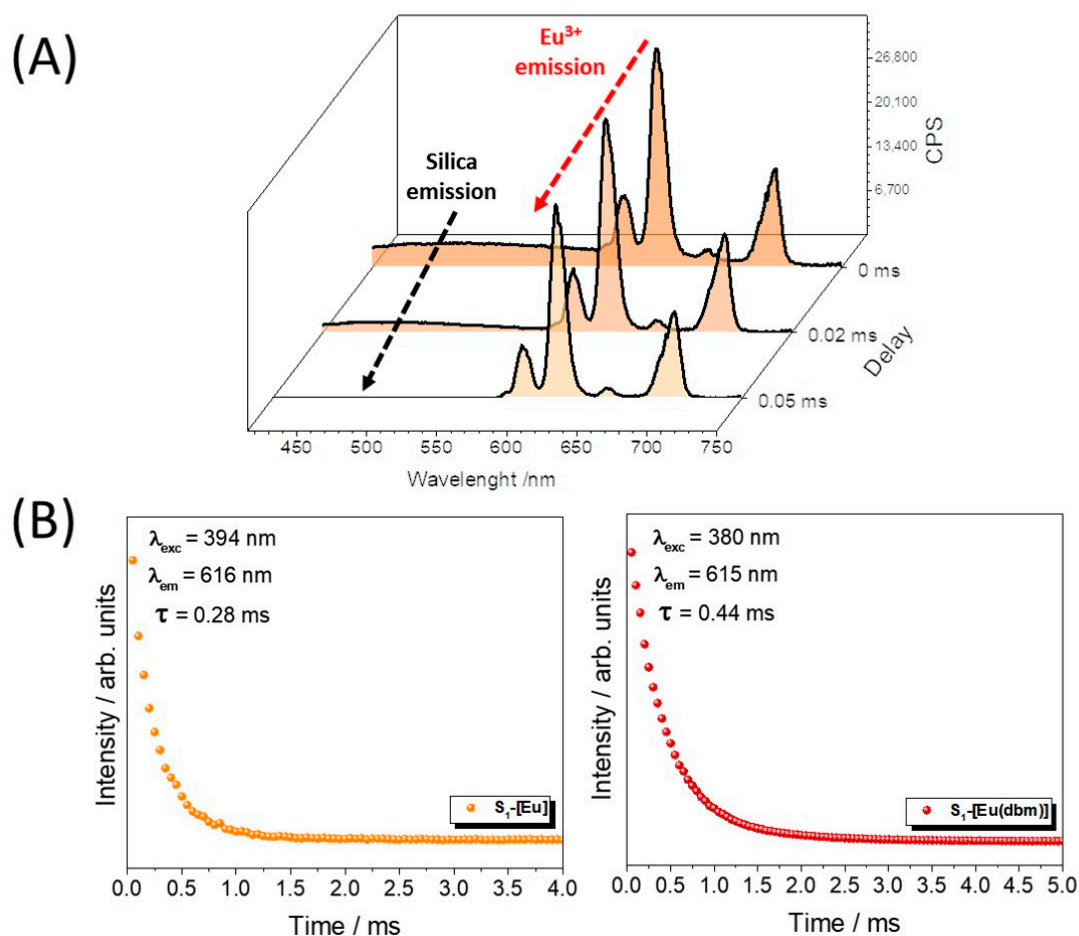


Figure 6. (A) Time-resolved emission spectra of S_1 -[Eu] with $\lambda_{exc} = 394$ nm; (B) 5D_0 excited state decay curves of S_1 -[Eu] and S_1 -[Eu(dbm)].

Table 2. 5D_0 excited state lifetime (τ), radiative (A_{rad}) and nonradiative (A_{nrad}) decay ratios, intrinsic emission quantum yield (ϕ_{Ln}^{Ln}) and the number of coordinated H_2O molecules (q_{H_2O}) for S_1 -[Eu] and S_1 -[Eu(dbm)].

Sample	τ /ms	A_{rad}/s^{-1}	A_{nrad}/s^{-1}	ϕ_{Ln}^{Ln}	q_{H_2O}
S_1 -[Eu]	0.28	398	3225	11	3.5
S_1 -[Eu(dbm)]	0.44	864	1387	38	1.6

Moreover, from τ values, it is possible to estimate the number of water molecules (q_{H_2O}) coordinated to Eu^{3+} by using the Horrocks and Sudnick model [57] (Equation (3)), where τ_{H_2O} is the 5D_0 state lifetime of the hybrid in water suspension.

$$q_{H_2O} = 1.05 \times \left[\frac{1}{\tau_{H_2O}} - \left(A_{01} \times \frac{\sum S_{0j}}{S_{01}} \right) \right]. \quad (3)$$

After the dbm^- coordination to Eu^{3+} , τ , A_{rad} and ϕ_{Ln}^{Ln} increases, in accordance with the Eu^{3+} sensitizing by the ligand. Moreover, the stoichiometric number of water molecules bonded to Eu^{3+} decreases from 3.5 to 1.6 after the dbm^- coordination, which agrees with the fact that dbm^- replaces H_2O molecules. This leads to a decrease of the multiphonon quenching of the 5D_0 stated, as it is indicated by the decrease of A_{nrad} .

Emission-decay curves display multiexponential behavior, suggesting that there are more than one non-equivalent Eu^{3+} local sites, which agrees with the literature [12,58]. In this sense, by combining

this information and the fact that Eu^{3+} is coordinated in a bidentate way to the carboxylate groups (as concluded by FTIR analysis), it is feasible to propose the structures shown in Figure 7 for Eu^{3+} local sites on the SiO_2 particle surface. In those cases, the coordination number of Eu^{3+} is seven or nine.

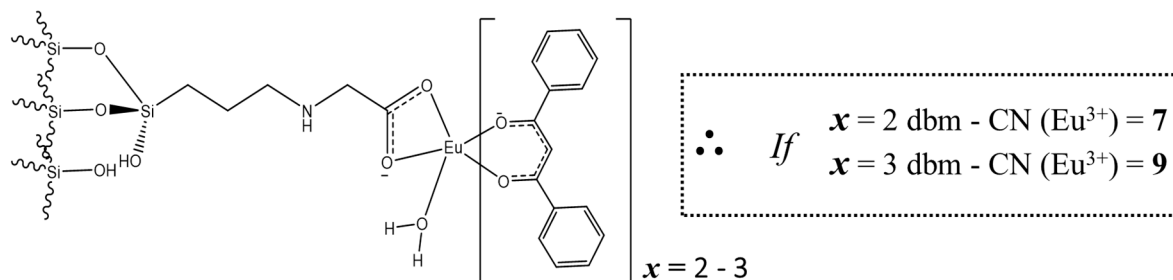


Figure 7. Eu^{3+} local sites on the SiO_2 surface with coordination number (CN) seven or nine.

By using ϕ_{Ln}^{Ln} as a figure of merit within the state-of-the-art of biomarkers fabricated by using covalently-bonded Ln^{3+} -based hybrids, Table 3, the value reported by us is among the best and only few materials [59–62] feature higher values. Therefore, the finds reported here confirm that the step-by-step process was successful to synthesize violet/blue-to-red downshifting emitting S_1 -[Eu(dbm)] hybrids featuring high emission color purity and high intrinsic emission quantum yield, displaying potential for application as a luminescent biomarker.

Table 3. State-of-the-art of luminescent hybrids containing dbm^- ligands coordinated to Eu^{3+} comparing ϕ_{Ln}^{Ln} as a figure of merit.

System	[ref]	Ligands	Host	ϕ_{Ln}^{Ln}
Phen-Eu-DBM- SiO_2/ZnO	[59]	dbm^- and phen	ZnO/SiO_2	55.3
Eu-DBM- SiO_2/ZnO	[59]	dbm^-	ZnO/SiO_2	22.6
Si12N-EDTAEu-dbm	[60]	EDTA modified and dbm^-	Silica Gel (commercial)	52.3
SiO_2 -APTES-cpa-Eu(DBM) ₃	[61]	dbm^-	Mesoporous silica	41.1
Sample C	[62]	dbm^-	ORMOSILs	39.2
Eu(DBMSi-SBA-15) ₃ phen	[63]	dbm^- and phen	Mesoporous silica	32.7
bpy-Eu-DBM-S16	[64]	dbm^- and 2,2'-bipyridine	Mesoporous silica	7.7
SiO_2 -[Eu(SB)(dbm) _y]	[12]	Schiff base and dbm^-	Dense silica	32.0
Eu(DBM-SBA-15) ₃ PMMA	[65]	dbm^- and PMMA ² polymer	Mesoporous silica	10.5
SiO_2 @Eu-DBM	[66]	dbm^-	Mesoporous silica	14.0
Eu(ZnO-MAA-PHEMA-SBA-15)(DBM) ₃	[67]	dbm^- and silylated polymer	Mesoporous silica	22.3
Fe_3O_4 [@ SiO_2]1NEu	[68]	EDTA modified and dbm^-	Fe_3O_4 @ SiO_2	36.0
Eu(Dbms-Si) ₃ Phen/ SiO_2	[69]	dbm^- and phen	Silica	9.0
S_1 -[Eu(dbm)]	This study	dbm^- and carboxylic acid	Dense silica	38.4

phen = 1,10-phenanthroline; PMMA = poly(methyl methacrylate); PHEMA = poly 2-hydroxyethyl methacrylate; EDTA = ethylenediaminetetraacetic acid; ORMOSILs = Organically modified silicates.

To confirm this potentially, preliminary bioimaging tests were performed using fluorescence microscopy to investigate the interaction between the final hybrid S_1 -[Eu(dbm)] and CHO-k1 cells. Figure S5 shows the fluorescence microscopy images of CHO-k1 marked with DAPI blue-emitting nuclear stain and the red-emitting S_1 -[Eu(dbm)] hybrid. The tests were performed by exposing the cells to the hybrid for 2 h at concentrations of 62.5 and 125 $\mu\text{g}/\text{mL}$ (for further details, see Note S1) [12,33]. The images in Figure S5 suggest that the hybrid was internalized by cells, crossing the cellular membrane and localized in intracellular regions at both concentrations tested. Besides, it was possible to confirm that the material keeps its luminescence in the red region even inside the cellular environment, suggesting that the medium does not cause changes in the hybrid structure and that it remains stable under physiological conditions. These preliminary characteristics corroborate that the material has potential for application in the field of bioimaging.

4. Conclusions

Herein, nanospheres of SiO₂—average size of 32 nm—decorated with luminescent Eu³⁺-dbm complexes bonded by carboxylic bridges were successfully synthesized by a step-by-step method. The combination of thermogravimetry, FTIR, ²⁹Si NMR and luminescence spectroscopy by using Eu³⁺ as a spectroscopic probe confirmed at least two non-equivalent Eu³⁺ local sites onto the SiO₂ surface composed by Eu³⁺ bonded to two or three dbm⁻ ligands. The fabricated hybrid also matches (i) broad excitation band within the violet/blue spectral window, favoring the hybrid excitation using lower energy than the traditional UV applied in biological assays, (ii) intrinsic emission quantum yield (38%) among the best values reported so far for Eu³⁺-dbm based hybrids and (iii) intense red light emission featuring high emission color purity and relatively-long lifetime (0.44 ms). The results observed by fluorescence microscopy indicated that the hybrid was able to cross the cellular membrane and at the cytoplasm did not lose its red luminescence. Therefore, those finds confirm that this hybrid displays the potential to be applied as a biomarker for several imaging techniques such as time-resolved luminescence microscopy and confocal/fluorescence microscopy.

Supplementary Materials: The following are available online at <http://www.mdpi.com/1996-1944/13/23/5494/s1>, Figure S1. Histograms showing the diameter and standard deviation of the samples (A) S₁ and (B) S₁-[Eu(dbm)]. EDS spectra of (C) S₁ e (D) S₁-[Eu(dbm)]. (E) Surface chemical mapping of S₁-[Eu(dbm)] suggesting a homogenous distribution of Si and Eu; Figure S2. FTIR spectra of all synthesized samples (left); magnification within the 1800–1300 cm⁻¹ range (middle) and magnification within the 900–850 cm⁻¹ range (right); Table S1. Position of the symmetric (ν_s) and antisymmetric (ν_{as}) stretching vibrations to determine the coordination modes of the carboxylate groups to Eu³⁺. Figure S3. (A) Qualitative test using ninhydrin to identify and compare the presence of primary amines in S₁N and S₁NC; (B) Calibration curve using APTES and ninhydrin. Figure S4. Thermogravimetric (TG) and first derivate (DTG) curves of all samples. Table S2. Weight loss assigned to the two thermal events obtained from the comparison of TG and DTG curves. **Note S1.** Slide preparation protocol for analysis by fluorescence microscopy. **Figure S5.** Fluorescence microscopy images of CHO-k1 rat cells cultivated in a suspension of 62.5 (top) and 125 µg/mL (bottom) of S₁-[Eu(dbm)] and DAPI nuclear stain, using 40x of magnification and lens aperture of 0.95. (A and D) Excitation with laser 405 nm and read in the DAPI channel - blue; (B and E) excitation with laser 561 nm and read in the Texas Red channel - red; (C) overlapping images A and B; (F) overlapping images D and E.

Author Contributions: Conceptualization, J.A.O.S., A.M.G.M., A.G.B.-J., A.M.P. and S.A.M.L.; Methodology, J.A.O.S. and A.M.G.M.; Validation, A.M.G.M. and A.M.P.; Formal Analysis, J.A.O.S.; Investigation, J.A.O.S. and S.A.M.L.; Resources, A.M.P. and S.A.M.L.; Writing—Original Draft Preparation, J.A.O.S., A.M.G.M. and A.G.B.-J.; Writing—Review & Editing, A.M.P. and S.A.M.L.; Visualization, J.A.O.S. and A.M.G.M.; Supervision, A.M.G.M., A.M.P. and S.A.M.L.; Project Administration, S.A.M.L.; Funding Acquisition, A.M.P. and S.A.M.L. All authors have read and agreed to the published version of the manuscript.

Funding: The authors are thankful to the Brazilian agencies CAPES, CNPq (Grant number 307385/2015-9) and São Paulo Research Foundation, FAPESP (Grant numbers FAPESP 2014/04907-3; FAPESP 2019/26103-7; FAPESP 2020/14749-7).

Acknowledgments: The following laboratories are acknowledged for their contribution to the sample characterizations: Laboratório de Microscopia Avançada, LMA (IQ-UNESP); Laboratório Multiusuários de Ressonância Magnética Nuclear (IQ-UNESP); Núcleo de Inovação Tecnológica em Borracha Natural (FCT-UNESP); Grupo SOL-GEL (Eduardo José Nassar, UNIFRAN); Laboratório de Gestão e Caracterização de Resíduos Sólidos, LGCRS (Sílvia Rainho Teixeira, FCT-UNESP); Laboratório de Materiais Nanoestruturados para Análises Ambientais e Biológicas (Carlos J. L. Constantino, FCT-UNESP, FAPESP 2013/14262-7); Laboratório de Materiais Magnéticos e Coloides (Miguel Jafelicci, IQ-UNESP).

Conflicts of Interest: The authors declare no conflict of interest.

References

1. Sábio, R.M.; Santagneli, S.H.; Gressier, M.; Caiut, J.M.A.; Pazin, W.M.; Leite, I.S.; Inada, N.M.; Da Silva, R.R.; Ribeiro, S.J.L.; Menu, M.J. Luminescent nanohybrids based on silica and silylated Ru(II)-Yb(III) heterobinuclear complex: New tools for biological media analysis. *Nanotechnology* **2020**, *31*, 085709. [[CrossRef](#)] [[PubMed](#)]
2. Monteiro, J.H.S.K. Recent advances in luminescence imaging of biological systems using lanthanide (III) luminescent complexes. *Molecules* **2020**, *25*, 2089. [[CrossRef](#)] [[PubMed](#)]

3. Ranjan, S.; Jayakumar, M.K.G.; Zhang, Y. Luminescent lanthanide nanomaterials: An emerging tool for theranostic applications. *Nanomedicine* **2015**, *10*, 1477–1491. [[CrossRef](#)] [[PubMed](#)]
4. Chinnathambi, S.; Shirahata, N. Recent advances on fluorescent biomarkers of near-infrared quantum dots for in vitro and in vivo imaging. *Sci. Technol. Adv. Mater.* **2019**, *20*, 337–355. [[CrossRef](#)]
5. Reddy, M.L.P.; Divya, V.; Pavithran, R. Visible-light sensitized luminescent europium (III)- β -diketonate complexes: Bioprobes for cellular imaging. *Dalton Trans.* **2013**, *42*, 15249–15262. [[CrossRef](#)]
6. Chen, Y. Fluorescent probes for detection and bioimaging of leucine aminopeptidase. *Mater. Today Chem.* **2020**, *15*, 100216. [[CrossRef](#)]
7. Pandey, S.; Bodas, D. High-quality quantum dots for multiplexed bioimaging: A critical review. *Adv. Colloid Interface Sci.* **2020**, *278*, 102137. [[CrossRef](#)]
8. Bai, Y.; Shu, T.; Su, L.; Zhang, X. Fluorescent gold nanoclusters for biosensor and bioimaging application. *Crystals* **2020**, *10*, 357. [[CrossRef](#)]
9. Li, H.; Yan, X.; Kong, D.; Jin, R.; Sun, C.; Du, D.; Lin, Y.; Lu, G. Recent advances in carbon dots for bioimaging applications. *Nanoscale Horiz.* **2020**, *5*, 218–234. [[CrossRef](#)]
10. Jaque, D.; Richard, C.; Viana, B.; Soga, K.; Liu, X.; Solé, J.G. Inorganic nanoparticles for optical bioimaging. *Adv. Opt. Photon.* **2016**, *8*, 1–103. [[CrossRef](#)]
11. Zhao, Q.; Huang, C.; Li, F. Phosphorescent Heavy-Metal Complexes for Bioimaging. *Chem. Soc. Rev.* **2011**, *40*, 2508–2524. [[CrossRef](#)] [[PubMed](#)]
12. Mutti, A.M.G.; Santos, J.A.O.; Cavalcante, D.G.S.M.; Gomes, A.S.; Job, A.E.; Teixeira, G.R.; Pires, A.M.; Lima, S.A.M. Design of a red-emitter hybrid material for bioimaging: Europium complexes grafted on silica particles. *Mater. Today Chem.* **2019**, *14*, 100204. [[CrossRef](#)]
13. Bünzli, J.C.G. Lanthanide light for biology and medical diagnosis. *J. Lumin.* **2016**, *170*, 866–878. [[CrossRef](#)]
14. Binnemans, K. Lanthanide-based luminescent hybrid materials. *Chem. Rev.* **2009**, *109*, 4283–4374. [[CrossRef](#)]
15. Sun, J.; Song, B.; Ye, Z.; Yuan, J. Mitochondria targetable time-gated luminescence probe for singlet oxygen based on a β -diketonate-europium complex. *Inorg. Chem.* **2015**, *54*, 11660–11668. [[CrossRef](#)]
16. Lima, P.P.; Sá Ferreira, R.A.; Freire, R.O.; Almeida Paz, F.A.; Fu, L.; Alves, S.; Carlos, L.D.; Malta, O.L. Spectroscopic study of a UV-photostable organic-inorganic hybrids incorporating an Eu^{3+} β -diketonate complex. *Chem. Phys. Chem.* **2006**, *7*, 735–746. [[CrossRef](#)]
17. DeOliveira, E.; Neri, R.; Serra, O.A.; Prado, A.G.S. Antenna effect in highly luminescent Eu^{3+} anchored in hexagonal mesoporous silica. *Chem. Mater.* **2007**, *11*, 5437–5442. [[CrossRef](#)]
18. Lechevallier, S.; Jorge, J.; Silveira, R.M.; Ratel-Ramond, N.; Neumeyer, D.; Menu, M.J.; Gressier, M.; Marçal, A.L.; Rocha, A.L.; Martines, M.A.U.; et al. Luminescence properties of mesoporous silica nanoparticles encapsulating different europium complexes: Application for biolabelling. *J. Nanomater.* **2013**, *2013*, 1–12. [[CrossRef](#)]
19. Ma, J.; Yang, D.; Song, X.; Wang, Y. Luminescent materials of covalent grafting lanthanide complexes to the synthetic clays. *J. Lumin.* **2019**, 126–132. [[CrossRef](#)]
20. Kataoka, T.; Abe, S.; Tagaya, M. Surface-engineered design of efficient luminescent europium (III) Complex-based hydroxyapatite nanocrystals for rapid HeLa cancer cell imaging. *ACS Appl. Mater. Interfaces* **2019**, *11*, 8915–8927. [[CrossRef](#)]
21. Comby, S.; Surender, E.M.; Kotova, O.; Truman, L.K.; Molloy, J.K.; Gunnlaugsson, T. Lanthanide-functionalized nanoparticles as MRI and luminescent probes for sensing and/or imaging applications. *Inorg. Chem.* **2014**, *53*, 1867–1879. [[CrossRef](#)] [[PubMed](#)]
22. Costa, A.L.; Bispo, A.G., Jr.; Lima, S.A.M.; Pires, A.M. Multicolor-emitting luminescent $\text{Y}_2\text{O}_3:\text{RE}^{3+}@\text{SiO}_2-[\text{RE}^{3+}(\beta\text{-diketone})_3]$ core@shell hybrids featuring dual RE^{3+} activator centers. *J. Alloys Compd.* **2020**, *843*, 155811. [[CrossRef](#)]
23. Li, L.; Wang, W.; Tang, J.; Wang, Y.; Liu, J.; Huang, L.; Wang, Y.; Guo, F.; Wang, J.; Shen, W.; et al. Classification, synthesis and application of luminescent silica nanoparticles: A review. *Nanoscale Res. Lett.* **2019**, *14*, 190. [[CrossRef](#)] [[PubMed](#)]
24. De Oliveira, L.F.; Bouchmella, K.; Goncalves, K.A.; Bettini, J.; Kobarg, J.; Cardoso, M.B. functionalized silica nanoparticles as an alternative platform for targeted drug-delivery of water insoluble drugs. *Langmuir* **2016**, *32*, 3217–3225. [[CrossRef](#)] [[PubMed](#)]
25. Azevedo, C.B.; Batista, T.M.; de Faria, E.H.; Rocha, L.A.; Ciuffi, K.J.; Nassar, E.J. Nanospherical silica as luminescent markers obtained by sol-gel. *J. Fluoresc.* **2015**, *25*, 433–440. [[CrossRef](#)]

26. Maturi, F.E.; Sábio, R.M.; Silva, R.R.; Lahoud, M.G.; Meneguín, A.B.; Valente, G.T.; Caface, R.A.; Leite, I.; Inada, N.M.; Ribeiro, S.J.L. Luminescent mesoporous silica nanohybrid based on drug derivative terbium complex. *Materials* **2019**, *16*, 933. [[CrossRef](#)]
27. Malba, C.; Sudhakaran, U.P.; Borsacchi, S.; Geppi, M.; Enrichi, F.; Natile, M.M.; Armelao, L.; Finotto, T.; Marin, R.; Riello, P.; et al. Structural and photophysical properties of rare-earth complexes encapsulated into surface modified mesoporous silica nanoparticles. *Dalton Trans.* **2014**, *43*, 16183–16196. [[CrossRef](#)]
28. Fedorenko, S.; Gilmanova, D.; Mukhametshina, A.; Nizameev, I.; Kholin, K.; Akhmadeev, B.; Voloshina, A.; Sapunova, A.; Kuznetsova, S.; Daminova, A.; et al. Silica nanoparticles with dual visible–NIR luminescence affected by silica confinement of Tb (III) and Yb (III) complexes for cellular imaging application. *J. Mater. Sci.* **2019**, *54*, 9140–9154. [[CrossRef](#)]
29. Lourenço, A.V.S.; Kodaira, C.A.; Ramos-Sanchez, E.M.; Felinto, M.C.F.C.; Goto, H.; Gidlund, M.; Malta, O.L.; Brito, H.F. Luminescent material based on the [Eu(TTA)₃(H₂O)₂] complex incorporated into modified silica particles for biological applications. *J. Inorg. Biochem.* **2013**, *123*, 11–17. [[CrossRef](#)]
30. Ilibi, M.; de Queiroz, T.B.; Ren, J.; De Cola, L.; de Camargo, A.S.S.; Eckert, H. Luminescent hybrid materials based on covalent attachment of Eu (III)—tris (bipyridinedicarboxylate) in the mesoporous silica host MCM-41. *Dalton Trans.* **2014**, *43*, 8318–8330. [[CrossRef](#)] [[PubMed](#)]
31. Li, Q.-F.; Yue, D.; Lu, W.; Zhang, X.; Li, C.; Wang, Z. Hybrid luminescence materials assembled by [Ln(DPA)₃]³⁻ and mesoporous host through ion-pairing interactions with high quantum efficiencies and long lifetimes. *Sci. Rep.* **2015**, *5*, 1–9. [[CrossRef](#)] [[PubMed](#)]
32. Zheng, X.; Wang, M.; Li, Q. Synthesis and luminescent properties of europium complexes covalently bonded to hybrid materials based on MCM-41 and poly (ionic liquids). *Materials* **2018**, *11*, 677. [[CrossRef](#)] [[PubMed](#)]
33. Mutti, A.M.G.; Santos, J.A.O.; Cavalcante, D.G.S.M.; Gomes, A.S.; Job, A.E.; Pires, A.M.; Lima, S.A.M. Decorated silica particles with terbium complexes as luminescent biomarker for cell imaging. *Opt. Mater.* **2019**, *90*, 57–63. [[CrossRef](#)]
34. Duarte, A.P.; Mauline, L.; Gressier, M.; Dexpert-Ghys, J.; Roques, C.; Caiut, J.M.A.; Deffune, E.; Maia, D.C.G.; Carlos, I.Z.; Ferreira, A.A.P.; et al. Organosilylated complex [Eu(TTA)₃(Bpy-Si)]: A bifunctional moiety for the engineering of luminescent silica-based nanoparticles for bioimaging. *Langmuir* **2013**, *29*, 5878–5888. [[CrossRef](#)] [[PubMed](#)]
35. An, Y.; Chen, M.; Xue, Q.; Liu, W. Preparation and self-assembly of carboxylic acid-functionalized silica. *J. Colloid Interface Sci.* **2007**, *311*, 507–513. [[CrossRef](#)] [[PubMed](#)]
36. Feinle, A.; Leichtfried, F.; Straßer, S.; Hüsing, N. Carboxylic acid-functionalized porous silica particles by a co-condensation approach. *J. Sol. Gel Sci. Technol.* **2017**, *81*, 138–146. [[CrossRef](#)]
37. Han, L.; Terasaki, O.; Che, S. Carboxylic group functionalized ordered mesoporous silicas. *J. Mater. Chem.* **2011**, *21*, 11033–11039. [[CrossRef](#)]
38. Janicki, R.; Mondry, A.; Starynowicz, P. Carboxylates of rare earth elements. *Coord. Chem. Rev.* **2017**, *340*, 98–133. [[CrossRef](#)]
39. Stöber, W.; Fink, A.; Bohn, E. Controlled growth of monodisperse silica spheres in the micron size range. *J. Colloid Interface Sci.* **1968**, *26*, 62–69. [[CrossRef](#)]
40. Socrates, G. *Infrared and Raman Characteristic Group Frequencies*, 3rd ed.; John Wiley & Sons, Ltd.: Chichester, UK, 2001; pp. 1–347. ISBN 0-470-09307-2.
41. Chandra, S.; Beaune, G.; Shirahata, N.; Winnik, F.M. A one-pot synthesis of water soluble highly fluorescent silica nanoparticles. *J. Mater. Chem. B* **2017**, *5*, 1363–1370. [[CrossRef](#)]
42. Ajloo, D.; Eslami Moghadam, M.; Ghadimi, K.; Ghadamgahi, M.; Saboury, A.A.; Divsalar, A.; Sheikhmohammadi, M.; Yousefi, K. Synthesis, characterization, spectroscopy, cytotoxic activity and molecular dynamic study on the interaction of three palladium complexes of phenanthroline and glycine derivatives with calf thymus DNA. *Inorg. Chim. Acta* **2015**, *430*, 144–160. [[CrossRef](#)]
43. Hozhabr, S.; Entezari, M.H. Amino-functionalized silica magnetite nanoparticles for the simultaneous removal of pollutants from aqueous solution. *Appl. Surf. Sci.* **2015**, *333*, 68–77. [[CrossRef](#)]
44. Deacon, G.; Phillips, R.J. Relationships between the carbon-oxygen stretching frequencies of carboxylate complexes and the type of carboxylate coordination. *Coord. Chem. Rev.* **1980**, *33*, 227–250. [[CrossRef](#)]
45. Rocha, L.A.; Freiria, J.D.C.; Caiut, J.M.A.; Ribeiro, S.J.L.; Messaddeq, Y.; Verelst, M.; Dexpert-Ghys, J. Luminescence properties of Eu-complex formations into ordered mesoporous silica particles obtained by the spray pyrolysis process. *Nanotechnology* **2015**, *26*, 335604. [[CrossRef](#)] [[PubMed](#)]

46. Rasband, W. *ImageJ*; Version 1.53e; Java 1.8.0_112 (64 Bit); National Institute of Health: Bethesda, MD, USA; Available online: https://imagej.net/Wayne_Rasband (accessed on 12 November 2020).
47. Keshavan, B.; Chandrashekara, P.G.; Gowda, N.M.M. Synthesis, characterization and spectral studies of lanthanide (III) nitrate complexes of promethazine. *J. Mol. Struct.* **2000**, *553*, 193–197. [[CrossRef](#)]
48. Qian, J.; Wang, Y.; Gao, X.; Zhan, Q.; Xu, Z.; He, S. Carboxyl-functionalized and bio-conjugated silica-coated quantum dots as targeting probes for cell imaging. *J. Nanosci. Nanotechnol.* **2010**, *10*, 1668–1675. [[CrossRef](#)] [[PubMed](#)]
49. Yang, S.; Li, W.; Cao, B.; Zeng, H.; Cai, W. Origin of blue emission from silicon nanoparticles: Direct transition and interface recombination. *J. Phys. Chem. C* **2011**, *115*, 21056–21062. [[CrossRef](#)]
50. Santa-Cruz, P.A.; Teles, F.S. *Spectra Lux Software, Version 2.0*; Ponto Quântico Nanodispositivos: Recife, Brazil, 2003.
51. Binnemans, K. Interpretation of europium (III) spectra. *Coord. Chem. Rev.* **2015**, *295*, 1–45. [[CrossRef](#)]
52. Beeby, A.; Clarkson, I.M.; Dickins, R.S.; Faulkner, S.; Parker, D.; Royle, L.; de Sousa, A.S.; Williams, J.A.G.; Woods, M. Non-radiative deactivation of the excited states of europium, terbium and ytterbium complexes by proximate energy-matched OH, NH and CH oscillators: An improved luminescence method for establishing solution hydration states. *J. Chem. Soc. Perkin Trans. 2* **1999**, *3*, 493–504. [[CrossRef](#)]
53. Bispo-Jr, A.G.; Shinohara, G.M.M.; Pires, A.M.; Cardoso, C.X. Red phosphor based on Eu^{3+} -doped $\text{Y}_2(\text{MoO}_4)_3$ incorporated with Au NPs synthesized via Pechini's method. *Opt. Mater.* **2018**, *84*, 137–145. [[CrossRef](#)]
54. Bünzli, J.C.G. Lighting up cells with lanthanide self-assembled helicates. *Interface Focus* **2013**, *3*, 20130032. [[CrossRef](#)] [[PubMed](#)]
55. Wong, K.-L.; Bünzli, J.-C.G.; Tanner, P.A. Quantum yield and brightness. *J. Lumin.* **2020**, *224*, 117256. [[CrossRef](#)]
56. Lide, D.R. (Ed.) *CRC Handbook of Chemistry and Physics*, 84th ed.; RC Press: Boca Raton, FL, USA, 2003; ISBN 0-8493-0484-9.
57. Horrocks, W.D.; Sudnick, D.R. Lanthanide ion luminescence probes of the structure of biological macromolecules. *Acc. Chem. Res.* **1981**, *14*, 384–392. [[CrossRef](#)]
58. Da Rosa, P.P.F.; Kitagawa, Y.; Hasegawa, Y. Luminescent lanthanide complex with seven-coordination geometry. *Coord. Chem. Rev.* **2020**, *406*, 213153. [[CrossRef](#)]
59. Li, Y.-J.; Yan, B. Photophysical properties of a novel organic-inorganic hybrid material: Eu (III)- β -diketone complex covalently bonded to SiO_2/ZnO composite matrix. *Photochem. Photobiol.* **2010**, *86*, 1008–1015. [[CrossRef](#)]
60. Aguiar, F.P.; Costa, I.F.; Geraldo, J.; Espínola, P.; Faustino, W.M.; Moura, J.L.; Brito, H.F.; Paolini, T.B.; Cláudia, M.; Felinto, F.C.; et al. Luminescent hybrid materials functionalized with lanthanide ethylenodiaminetetraacetate complexes containing β -diketonate as antenna ligands. *J. Lumin.* **2016**, *170*, 538–546. [[CrossRef](#)]
61. Xu, J.; Sun, Z.; Jia, L.; Li, B.; Zhao, L.; Liu, X.; Ma, Y.; Tian, H.; Wang, Q.; Liu, W.; et al. Visible light sensitized attapulgite-based lanthanide composites: Microstructure, photophysical behaviour and biological application. *Dalton Trans.* **2011**, *40*, 12909–12916. [[CrossRef](#)]
62. Wang, Y.; Li, B.; Zhang, L.; Zuo, Q.; Liu, L.; Li, P. Improved photoluminescence properties of a novel Europium (III) complex covalently grafted to organically modified silicates. *J. Colloid Interface Sci.* **2010**, *349*, 505–511. [[CrossRef](#)]
63. Kong, L.L.; Yan, B.; Li, Y. Mesoporous hybrids containing Eu^{3+} complexes covalently bonded to SBA-15 functionalized: Assembly, characterization and photoluminescence. *J. Solid State Chem.* **2009**, *182*, 1631–1637. [[CrossRef](#)]
64. Li, Y.; Yan, B.; Li, Y. Hybrid materials of SBA-16 functionalized by rare earth (Eu^{3+} , Tb^{3+}) complexes of modified β -diketone (TTA and DBM): Covalently bonding assembly and photophysical properties. *J. Solid State Chem.* **2009**, *183*, 871–877. [[CrossRef](#)]
65. Li, Y.-J.; Yan, B.; Li, Y. Lanthanide (Eu^{3+} , Tb^{3+}) centered mesoporous hybrids with 1,3-diphenyl-1,3-propanepione covalently linking SBA-15 (SBA-16) and poly (methylacrylic acid). *Chem. Asian J.* **2010**, *5*, 1642–1651. [[CrossRef](#)] [[PubMed](#)]
66. Guo, X.; Canet, J.L.; Boyer, D.; Adumeau, P.; Mahiou, R. Luminescent thin films and nanoparticles of europium doped hybrids based on organosilyl β -diketonate. *J. Sol. Gel Sci. Technol.* **2012**, *64*, 404–410. [[CrossRef](#)]

67. Shao, Y.F.; Yan, B.; Jiang, Z.Y. Multicomponent assembly of luminescent hybrid materials of ZnO-lanthanide polymer complex functionalized SBA-15 mesoporous host by chemical bonds. *RSC Adv.* **2012**, *2*, 9192–9200. [[CrossRef](#)]
68. Pires, G.P.; Costa, I.F.; Brito, H.F.; Faustino, W.M.; Teotonio, E.E.S. Luminescent and magnetic materials with high content of Eu³⁺-EDTA complexes. *Dalton Trans.* **2016**, *45*, 10960–10968. [[CrossRef](#)]
69. Fadieiev, Y.M.; Smola, S.S.; Malinka, E.V.; Rusakova, N.V. Study of association of Eu (III) β -diketonato-1,10-phenanthroline complexes in silica-based hybrid materials. *J. Lumin.* **2017**, *183*, 121–128. [[CrossRef](#)]

Publisher's Note: MDPI stays neutral with regard to jurisdictional claims in published maps and institutional affiliations.



© 2020 by the authors. Licensee MDPI, Basel, Switzerland. This article is an open access article distributed under the terms and conditions of the Creative Commons Attribution (CC BY) license (<http://creativecommons.org/licenses/by/4.0/>).